Geophysical Journal International

Geophys. J. Int. (2015) **203,** 1864–1872 doi: 10.1093/gji/ggv407

GJI Geomagnetism, rock magnetism and palaeomagnetism

A new model of Earth's radial conductivity structure derived from over 10 yr of satellite and observatory magnetic data

Christoph Püthe,[1] Alexey Kuvshinov,[1] Amir Khan[1] and Nils Olsen[2]

[1]*Institute of Geophysics, ETH Zürich, Zürich, Switzerland. E-mail: christoph.puethe@erdw.ethz.ch*

[2]*DTU Space, Technical University of Denmark, Lyngby, Denmark*

Accepted 2015 September 21. Received 2015 September 14; in original form 2015 March 4

SUMMARY

We present a new model of the radial (1-D) conductivity structure of Earth's mantle. This model is derived from more than 10 yr of magnetic measurements from the satellites Ørsted, CHAMP, SAC-C and the *Swarm* trio as well as the global network of geomagnetic observatories. After removal of core and crustal field as predicted by a recent field model, we fit the magnetic data with spherical harmonic coefficients describing ring current activity and associated induction effects and estimate global *C*-responses at periods between 1.5 and 150 d. The *C*-responses are corrected for 3-D effects due to induction in the oceans and inverted for a 1-D model of mantle conductivity using both probabilistic and deterministic methods. Very similar results are obtained, consisting of a highly resistive upper mantle, an increase in conductivity in and beneath the transition zone and a conductive lower mantle. Analysis of the Hessian of the cost function reveals that the data are most sensitive to structures at depths between 800 and 1200 km, in agreement with the results obtained from the probabilistic approach. Preliminary interpretation of the inverted conductivity structure based on laboratory-based conductivity profiles shows that the recovered structure in the lower mantle either requires higher temperatures or the presence of material of high conductivity related to ponding of carbonate melts below the transition zone.

Key words: Time-series analysis; Geomagnetic induction; Magnetic and electrical properties; Composition of the mantle.

1 INTRODUCTION

The recovery of 1-D conductivity-depth profiles of Earth's mantle is an old geophysical problem that has been revisited many times over the past century, for example, by Chapman & Price (1930), Lahiri & Price (1939), Banks (1969), Schultz & Larsen (1987) and Olsen (1998). All of these studies were based on data from continental geomagnetic observatories. While this practice is expected to yield reliable results in local and regional studies, the results of global studies that aim at deriving laterally averaged conductivity profiles are inevitably biased towards continental regions. In contrast, low-Earth-orbit platforms provide high-quality magnetic data with almost uniform spatial coverage. However, the analysis of satellite data is challenging due to the difficulty in distinguishing between temporal and spatial variations in the records. Satellite data have been used to derive global 1-D conductivity models of Earth's mantle within the last three decades, for example, by Didwall (1984), Olsen (1999), Constable & Constable (2004), Velímský *et al.* (2006), Kuvshinov & Olsen (2006), Civet & Tarits (2013) and Civet *et al.* (2015).

In preparation for the *Swarm* multisatellite mission (Friis-Christensen *et al.* 2006), we developed a new method to recover the 1-D conductivity structure of Earth's mantle, which takes 3-D effects arising from the known distribution of oceans and continents into account (Püthe & Kuvshinov 2013). The elaborated concepts have now been applied to 10 yr (September 2000 to August 2010) of magnetic measurements of the satellites Ørsted, CHAMP and SAC-C, as well as the global network of geomagnetic observatories, in addition to eight months (December 2013 to July 2014) of data from the three *Swarm* satellites and the geomagnetic observatories. This is the largest data set ever used for a 1-D mantle conductivity study, and use of both satellite and observatory data combines the strengths of both data sources.

Geophysical inverse problems suffer from non-uniqueness. As a consequence, analysis of model resolution and accuracy is crucial, but difficult to address properly within the deterministic framework. Probabilistic inversion provides the foundation for such an analysis, but is computationally more expensive. In this study, we derive 1-D mantle conductivity models using both deterministic (Section 3) and probabilistic (Section 4) methods and show

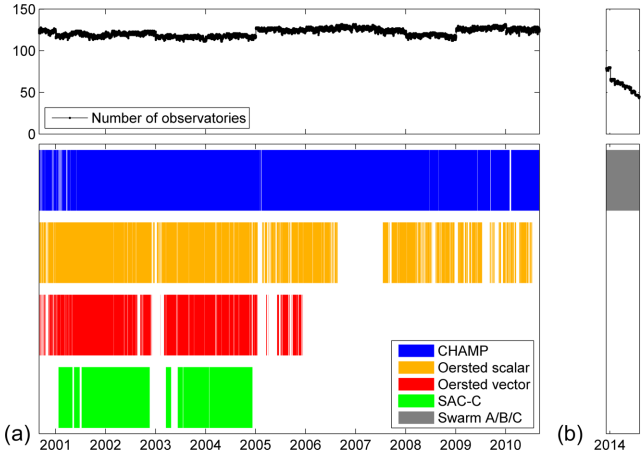

Figure 1. Availability of observatory and satellite data for the CHAMP phase (a) and the *Swarm* phase (b). The small amount of observatory data during the *Swarm* phase is due to the fact that many observatories had not yet published their measurements when this study was started.

that both approaches can be used to gain knowledge about model uncertainties.

2 DATA PROCESSING

2.1 Selection of the data

In total, we processed more than 10 yr of magnetic satellite and observatory data. The period from September 2000 to August 2010 will hereinafter be denoted as 'CHAMP phase', while that from December 2013 to July 2014 will be denoted as '*Swarm* phase'. Both names refer to the satellites providing vector data for the indicated period.

Hourly mean vector data from observatories were available for the entire CHAMP phase; the number of observatories for which data are available ranged between 111 and 132. Ørsted vector data were only available from September 2000 to December 2005, while scalar data could be retrieved (with considerable gaps) until the end of the CHAMP phase. SAC-C provided scalar data from January 2001 to December 2004. All satellite data used presently have minute resolution. Due to the different sampling rates, the amount of observatory data and satellite data are comparable. This is also the case for the *Swarm* phase, although the number of observatories providing data (dropping over time from 80 to a minimum of 43) is considerably smaller than for the CHAMP phase. Fig. 1 displays data availability during both phases.

The raw data were processed as follows. First, we removed core and crustal field as predicted by an extension of the CHAOS-4 magnetic field model (Olsen *et al.* 2014), which covers the entire time span relevant for this study. Obvious outliers and baseline jumps were, after careful inspection, removed manually. If necessary, remaining slow variations in the observatory data were removed by fitting low-degree polynomials to the time series. No such correction was applied to satellite data.

In order to reduce the influence of ionospheric currents (*Sq* system and polar electrojets), we only used night-time data (defined here by local-time between 19:00 and 05:00) and avoided latitudes $>55^\circ$. The remaining magnetic field variations are assumed to be due to a large-scale magnetospheric source that consists mainly of a ring current around the geomagnetic equator. The spatial structure of the magnetic field due to such a source can be described by the single spherical harmonic $Y_1^0 = \cos\vartheta$, with ϑ denoting colatitude. Its temporal evolution is characterized by the external coefficient ε_1^0 and its induced counterpart ι_1^0 (for details of the mathematical description, we refer to, for example, Schmucker 1985a,b). We fit the magnetic field variations with these coefficients in the time-domain in bins of 1 hr. Allowing for more coefficients, using longer bins or parametrizing the time-dependency with cubic splines (as done by Kuvshinov & Olsen 2006) did not change the results significantly.

2.2 Estimation and correction of transfer functions

From time series of ε_1^0 and ι_1^0, we estimated scalar Q-responses and transformed them to C-responses, as described in Püthe & Kuvshinov (2013). That study relied on coefficient time series provided by the Comprehensive Inversion (Sabaka *et al.* 2013). In this study, we estimated the coefficients from raw magnetic data as described above. The processing tools elaborated by Püthe & Kuvshinov (2013), however, are applicable in any case.

Transfer functions were first estimated separately for each of the two phases. For the CHAMP phase, we obtained C-responses at 27 periods between 1.5 and 150 d. This is the period range in which ring-current activity is known to be the dominant source of magnetic variations (e.g. Schmucker 1985b). Outside this range, the assumption of a source field described by Y_1^0 is not valid, which is why extensions to shorter and longer periods were avoided. For the *Swarm* phase, we were restricted to periods up to 25 d due to the shortness of the available time series. The results are presented in Fig. 2(a).

C-responses estimated for the CHAMP and *Swarm* phase agree fairly well for all frequencies. This is remarkable, considering the limited amount of data available in the *Swarm* phase. Even if uncertainties are clearly larger for the *Swarm* phase than for the CHAMP phase, reliable estimates of C-responses at periods up to 25 d are attainable from only 8 months of satellite and observatory data. When data from both phases are combined, the resulting C-responses only differ insignificantly from those obtained for the CHAMP phase. Squared coherencies exceed 0.9 throughout, justifying our assumptions about the source. The real part of C, which is a measure of the penetration depth (Weidelt 1972), increases monotonically from 700 to 1600 km.

We compare our results to those of Kuvshinov & Olsen (2006), who conducted a similar study based on 5 yr (2001–2005) of satellite magnetic data. Overall, results from the two studies are observed to agree fairly well. Our C-responses, however, are smoother, show smaller uncertainties and higher coherencies. This is most probably due to the larger data set used in this study. Additionally, Re C is consistently found to be larger than that determined by Kuvshinov & Olsen (2006). This is explained as follows: When fitting the magnetic data with coefficients ε_1^0 and ι_1^0, Kuvshinov & Olsen (2006) added a small damping parameter to stabilize the solution and obtain continuous time series of coefficients in spite of gap-bearing raw data. This damping, however, slightly biased the estimated C-responses towards smaller amplitudes. In contrast to Kuvshinov & Olsen (2006), we here employ observatory data in addition to satellite data. As a result, a stable estimation of the coefficients is possible for each instant, obviating the requirement for damping.

From hereon, we work with C-responses estimated from data from both phases. These responses, which we label $C^{\mathrm{obs}}(\omega)$, where ω denotes angular frequency, are known to be affected by induction in the oceans (e.g. Everett *et al.* 2003; Kuvshinov & Olsen 2005). We iteratively correct the real and the imaginary part of

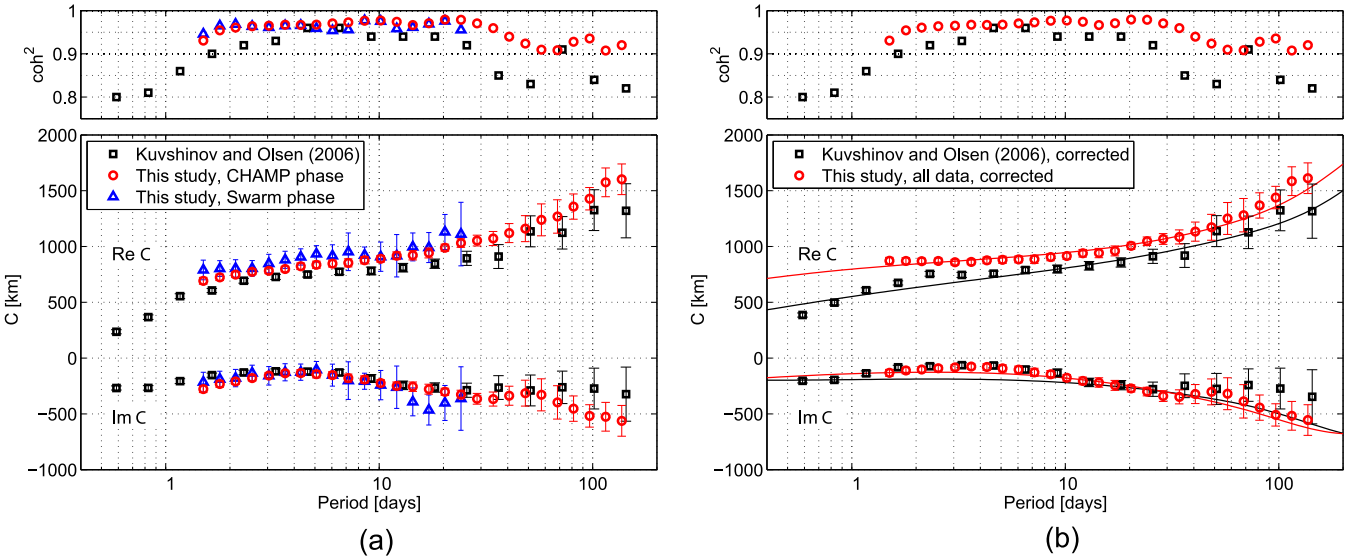

Figure 2. (a) Estimated (uncorrected) *C*-responses in this study in comparison to those obtained by Kuvshinov & Olsen (2006). (b) *C*-responses corrected for induction in the oceans; solid lines indicate *C*-response predictions corresponding to the recovered conductivity models (Fig. 5). Top panels show squared coherencies.

the *C*-responses for the ocean effect using

$$\mathrm{Re}\, C^{\mathrm{corr}}(\omega) = \mathrm{Re}\, C^{\mathrm{obs}}(\omega) \times \frac{\mathrm{Re}\, C^{1\text{-D}}(\omega)}{\mathrm{Re}\, C^{3\text{-D}}(\omega)}, \quad (1)$$

$$\mathrm{Im}\, C^{\mathrm{corr}}(\omega) = \mathrm{Im}\, C^{\mathrm{obs}}(\omega) \times \frac{\mathrm{Im}\, C^{1\text{-D}}(\omega)}{\mathrm{Im}\, C^{3\text{-D}}(\omega)}, \quad (2)$$

where $C^{1\text{-D}}(\omega)$ and $C^{3\text{-D}}(\omega)$ are the *C*-responses computed in a 1-D model and a 3-D model (consisting of a laterally heterogeneous surface shell plus the 1-D model underneath), respectively. This multiplicative scheme implies a relative correction of the estimated *C*-responses, which yields more reliable results than the absolute, additive correction previously used by Kuvshinov *et al.* (2005) and Püthe & Kuvshinov (2013). A separate treatment of Re *C* and Im *C* is necessary because a combined correction would be biased towards the real part, which has larger amplitudes. The entire correction scheme is presented in Fig. 3 (reprinted from Püthe & Kuvshinov 2013). Note that the scheme employs the deterministic inversion algorithm outlined in Section 3.1 to recover a 1-D mantle conductivity model in every iteration.

Corrected *C*-responses $C^{\mathrm{corr}}(\omega)$ are shown in Fig. 2(b) and compared to those obtained by Kuvshinov & Olsen (2006), who used a different correction scheme. The ocean effect is clearly visible in both the real and imaginary part at periods <10 d. Re C^{corr} remains almost constant at 850–900 km for periods up to 10 d. This implies a thick, highly resistive layer underneath the surface shell. The effect of the correction is slightly more pronounced than in the results of Kuvshinov & Olsen (2006); the differences (in the real part) therefore increase for periods <10 d. This is likely a result of the different correction scheme.

The numerical values of observed and corrected *C*-responses, uncertainties and squared coherencies are provided in Table 1.

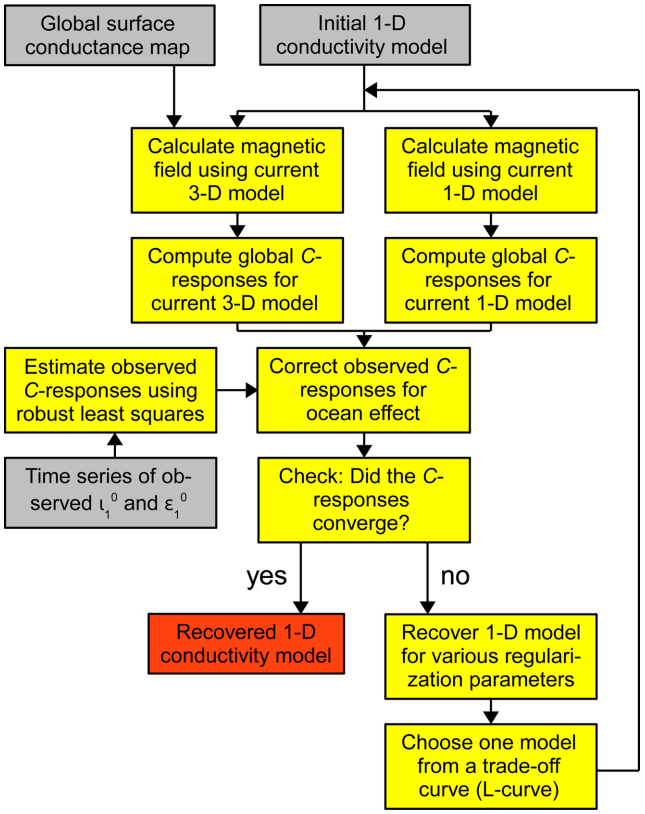

Figure 3. Processing scheme for the iterative 1-D inversion. Inputs and outputs are marked by grey and red boxes, respectively. Note that by the term '3-D model', we denote the 1-D model plus a laterally heterogeneous surface shell.

3 DETERMINISTIC INVERSION

3.1 1-D inversion: concept

Deterministic inversion seeks a single model **m** that minimizes the misfit between data and model predictions given additional constraints. It can be formulated as a minimization problem, in which the cost function (or penalty function) ϕ is defined as

$$\phi(\mathbf{m}, \lambda) = \phi_d(\mathbf{m}) + \lambda \phi_m(\mathbf{m}), \quad (3)$$

where ϕ_d is data misfit and λ and ϕ_m are regularization parameter and regularization term, respectively. The model vector **m** consists

Table 1. Observed and corrected C-responses with uncertainties (in km) and squared coherencies as functions of period (in seconds).

	C^{obs}		C^{corr}			
Period	Re C	Im C	Re C	Im C	δC^{obs}	coh^2
129600	692.3	−277.9	872.2	−132.3	43.5	0.93
154800	723.5	−232.5	870.7	−111.3	40.8	0.95
183600	748.4	−209.8	868.7	−102.6	37.5	0.96
219600	773.0	−179.2	870.3	−90.9	36.5	0.96
262800	781.8	−156.4	859.3	−83.4	35.4	0.97
313200	798.6	−135.4	861.7	−76.2	35.2	0.97
370800	822.9	−134.3	875.9	−80.2	41.9	0.97
439200	836.6	−144.6	881.0	−91.7	45.7	0.97
522000	847.1	−152.9	884.4	−102.9	43.1	0.97
619200	853.4	−179.0	885.1	−127.6	51.3	0.97
738000	877.2	−192.2	905.0	−144.6	46.0	0.98
878400	890.1	−223.7	914.6	−176.6	42.3	0.98
1044000	917.4	−248.9	939.4	−204.8	48.6	0.97
1242000	921.7	−256.3	941.4	−218.6	59.2	0.97
1476000	942.6	−278.3	960.5	−244.5	63.0	0.97
1756800	989.2	−302.3	1006.1	−272.2	45.4	0.98
2088000	1031.3	−326.7	1047.2	−300.0	54.5	0.98
2484000	1052.9	−364.5	1067.6	−340.1	68.3	0.97
2955600	1071.8	−367.6	1085.4	−347.4	89.1	0.96
3513600	1120.4	−337.3	1133.3	−322.1	121.1	0.94
4179600	1160.2	−314.3	1172.4	−302.7	164.2	0.92
4971600	1239.1	−329.3	1250.9	−319.3	202.5	0.91
5911200	1269.4	−397.2	1280.4	−387.2	211.8	0.91
7030800	1357.4	−453.0	1368.2	−443.6	160.1	0.93
8362800	1428.5	−518.3	1438.8	−509.2	141.8	0.94
9946800	1574.9	−525.7	1585.2	−517.8	182.3	0.91
11829600	1602.6	−562.4	1612.0	−554.9	194.3	0.92

of a discrete parametrization of the radial conductivity structure. We formulate the data misfit as

$$\phi_d = \frac{1}{N_\omega} \sum_\omega \frac{|C^{\text{mod}}(\omega) - C^{\text{obs}}(\omega)|^2}{\delta C^{\text{obs}}(\omega)^2}, \tag{4}$$

where N_ω is number of frequencies, $C^{\text{obs}}(\omega)$ are estimated C-responses (potentially corrected for the ocean effect), $\delta C^{\text{obs}}(\omega)$ are corresponding uncertainties, and $C^{\text{mod}}(\omega)$ are modelled C-responses. The regularization term ϕ_m in our implementation penalizes jumps in conductivity between adjacent layers.

Descent methods (e.g. Nocedal & Wright 2006) make use of the gradient $\nabla\phi$ (and often also of the Hessian $\mathbf{H}(\phi)$) to systematically move through the model space until a point is reached where ϕ is minimum. Here, we apply the full Newton method, in which the model is updated as

$$\mathbf{m}_{k+1} = \mathbf{m}_k - \alpha_k \mathbf{H}^{-1}(\phi_k)\nabla\phi_k, \tag{5}$$

where α_k determines the step length in an inexact line search (e.g. Nocedal & Wright 2006). We compute model predictions $C^{\text{mod}}(\omega)$, gradient and Hessian of the data misfit ϕ_d analytically as outlined in the Appendix.

Let us assume that ϕ has a minimum at $\mathbf{m}_0$. Since the gradient of ϕ at $\mathbf{m}_0$ vanishes, a second-order polynomial approximation reads

$$\phi(\mathbf{m}_0 + \Delta\mathbf{m}) \approx \phi(\mathbf{m}_0) + \frac{1}{2}\Delta\mathbf{m}^\top \mathbf{H}(\phi(\mathbf{m}_0))\Delta\mathbf{m}, \tag{6}$$

with $\Delta\mathbf{m}$ being a perturbation of $\mathbf{m}_0$. Let us define

$$\Delta\phi = \phi(\mathbf{m}_0 + \Delta\mathbf{m}) - \phi(\mathbf{m}_0) \tag{7}$$

as a maximum permissible perturbation of ϕ. Eq. (6) can then be rewritten as

$$\Delta\phi = \frac{1}{2}\Delta\mathbf{m}^\top \mathbf{H}(\phi(\mathbf{m}_0))\Delta\mathbf{m}. \tag{8}$$

For simplicity, we allow $C^{\text{mod}}(\omega)$ to deviate from $C^{\text{obs}}(\omega)$ within uncertainties $\delta C^{\text{obs}}(\omega)$. According to eq. (4), this yields $\Delta\phi = 1$.

In case of a diagonal Hessian, eq. (8) is easily solved for maximum perturbations of a model parameter m_j:

$$\Delta m_j = \sqrt{\frac{2\Delta\phi}{H(\phi(\mathbf{m}_0))_{jj}}}. \tag{9}$$

A diagonal Hessian, however, implies that there is no correlation between any two model parameters. This is very improbable for real-world problems. In the much more important case of a non-diagonal Hessian, a proxy for Δm_j is given by

$$\Delta m_j = \sqrt{2\Delta\phi H(\phi(\mathbf{m}_0))^{-1}_{jj}}, \tag{10}$$

where $H(\phi(\mathbf{m}_0))^{-1}_{jj}$ denotes the jth diagonal element of the inverse Hessian (Pankratov & Kuvshinov 2015). Note that the formulations (9) and (10) are only equivalent in case of a diagonal Hessian.

Whether diagonal or non-diagonal, the perturbations Δm_j can be interpreted as estimates of model uncertainties. In the present context, these estimates only approximate the true model uncertainties. First, the use of a second-order polynomial implies a linearization of a non-linear inverse problem around the minimum of the cost function. Second, the choice of $\Delta\phi = 1$ is heuristic, and there might be good reasons for other choices. Finally, the applied regularization has generated large covariances between model parameters, such that the bounds for the conductivity in a specific layer necessarily depend on the conductivity in all other layers. Nevertheless,

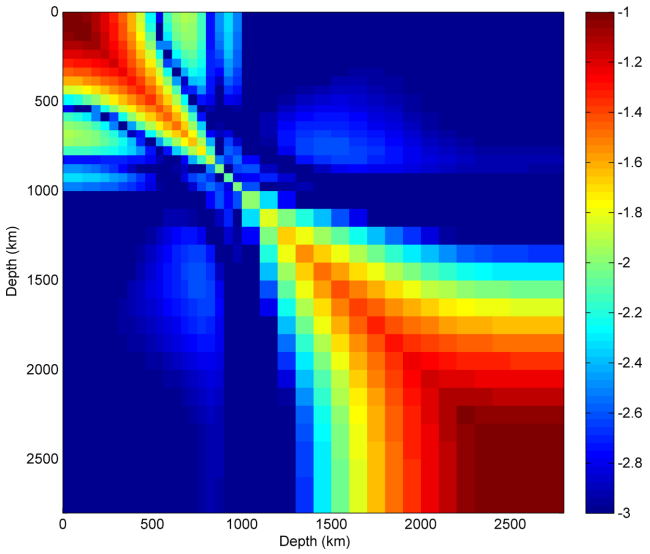

Figure 4. The inverse Hessian (absolute values, in logarithmic units) at the point of convergence $\mathbf{m}_0$. See the main text for details.

the perturbations Δm_j yield valuable information about *relative* uncertainties and thus about the resolution of the recovered model at different depths.

3.2 1-D inversion: implementation

The model is parametrized using $N = 40$ spherical layers in depth between Earth's surface and the core–mantle boundary (CMB) located at a depth of 2890 km. A very good conductor (of 10^5 S m^{-1}) is prescribed for the core. The thickness of the layers is generally fixed to 50 km at depths <1000 km and to 100 km underneath. Minor modifications of this rule permit layer boundaries at the main seismic discontinuities in the mid-mantle, located at depths of 410, 520 and 660 km, respectively.

We invert the corrected C-responses for several values of λ and manually pick the final results from an L-curve relating ϕ_d and ϕ_m (Hansen 1992). In practice, we choose the 'simplest' model, that is, the model with smallest ϕ_m, with the constraint $\phi_d < 1$. Fig. 4 shows the inverse Hessian at the point of convergence $\mathbf{m}_0$. The matrix is diagonally dominant, but contains significant energy in off-diagonal elements, implying correlations between the individual model parameters. We apply eq. (10) to calculate model uncertainties Δm_j.

Fig. 5 shows the recovered 1-D model with its uncertainties determined by analysis of the inverse Hessian. Also shown is the conductivity profile recovered from uncorrected C-responses and the result of Kuvshinov & Olsen (2006). The recovered model is characterized by a highly resistive zone in the top 400 km, with a minimum value of 2×10^{-3} S m^{-1} just beneath the surface shell. Conductivity increases steadily to a depth of 900 km, reaching a maximum of 2 S m^{-1}. The conductivity profile then shows a sharp edge; at greater depths, conductivity is almost constant, varying between 1 S m^{-1} and 2 S m^{-1} down to the CMB. The correction for the ocean effect has a great influence on the results in the top 600 km. As expected, the corrected C-responses correspond to a considerably more resistive conductivity model. This model is also significantly more resistive than that recovered by Kuvshinov & Olsen (2006) to a depth of 800 km.

The uncertainty estimates form an hourglass-shaped structure. Smallest uncertainties are observed at depths between 800 and 1200 km in line with the structure of the inverse Hessian (Fig. 4). At depths <400 km and >1600 km, conductivity is poorly constrained by the data.

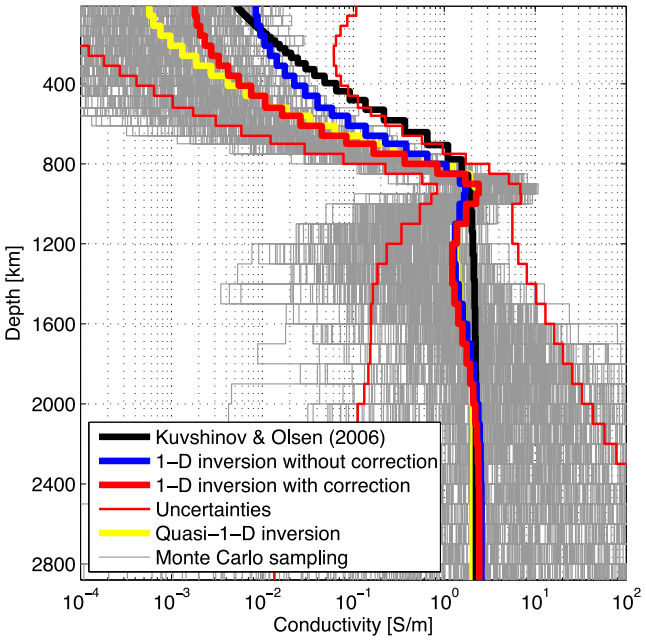

Figure 5. 1-D conductivity models recovered by Kuvshinov & Olsen (2006) (solid black line) and this study (1-D inversion without correction: solid blue line; 1-D inversion with correction: solid red line; quasi-1-D inversion: solid yellow line). Narrow red lines indicate uncertainties of the recovered (corrected) model, estimated from analysis of the inverse Hessian. In grey, we show 400 near-independent models obtained from Monte Carlo sampling.

Table 2. Conductivity model obtained from deterministic 1-D inversion (with correction for the ocean effect). Depth (to the top of the respective layer) in km, and conductivity in S m^{-1}.

Depth	Conductivity	Depth	Conductivity
0	1.814e−03	950	2.344e+00
10	1.829e−03	1000	1.815e+00
60	1.918e−03	1100	1.401e+00
110	2.085e−03	1200	1.232e+00
160	2.348e−03	1300	1.206e+00
210	2.737e−03	1400	1.269e+00
260	3.304e−03	1500	1.388e+00
310	4.136e−03	1600	1.542e+00
360	5.378e−03	1700	1.710e+00
410	7.290e−03	1800	1.874e+00
460	1.034e−02	1900	2.019e+00
520	1.559e−02	2000	2.136e+00
560	2.460e−02	2100	2.224e+00
610	4.158e−02	2200	2.284e+00
660	7.604e−02	2300	2.322e+00
700	1.497e−01	2400	2.344e+00
750	3.248e−01	2500	2.356e+00
800	7.490e−01	2600	2.360e+00
850	1.596e+00	2700	2.362e+00
900	2.412e+00	2800	2.362e+00

The conductivity model recovered in the deterministic inversion is provided in Table 2.

3.3 Quasi-1-D inversion

In the previous sections, we showed how to correct the estimated responses for 3-D effects due to induction in the oceans by an iterative

approach, and how to invert the corrected responses for 1-D conductivity structure. Although this approach has proven successful, a more natural and consistent treatment of 3-D effects is given by inverting the (uncorrected) responses directly in a 3-D environment.

We modified an existing modular 3-D inversion code (Püthe & Kuvshinov 2014) to invert for 1-D structure in the presence of a heterogeneous surface shell. For consistency with the existing implementation, the modified code does not invert C-responses, but the corresponding Q-responses. In a 3-D environment, model predictions, gradient and Hessian of the data misfit cannot be computed analytically as in the 1-D case. For the solution of the forward problem we hence employ a numerical procedure, which is based on a contracting integral-equation approach (Pankratov *et al.* 1995). The gradient is computed with finite differences, which requires N additional forward computations per iteration. A quasi-Newton method (e.g. Nocedal & Wright 2006) is employed to find the minimum of the cost function ϕ. As in the 1-D case, ϕ includes a regularization term that minimizes jumps between adjacent layers.

We applied the modified 3-D inversion code to the uncorrected Q-responses. The results for an appropriate regularization parameter are shown in Fig. 5. At depths >400 km, the result agrees perfectly with that of the iterative 1-D inversion. At shallower depths, the result of the direct inversion is slightly more resistive, but well within uncertainties. The very good agreement of the results confirms the functionality of the iterative approach, which is computationally less expensive than the direct method. It also justifies the more pronounced effect of the correction compared to that of Kuvshinov & Olsen (2006), *cf.* Fig. 2.

4 PROBABILISTIC INVERSION

4.1 Definitions

In contrast to deterministic inversion, probabilistic or Bayesian inversion (e.g. Tarantola 2005) does not seek a single model that explains data. Instead, it explores the parameter space and generates a multitude of models that can be analysed statistically.

Central to the Bayesian approach to inverse problems is the use of probability density functions (pdfs) to describe any piece of information entering the problem. We define a *prior* pdf $\rho(\mathbf{m})$, which contains information about the model that is independent of data, a *likelihood function* $\mathcal{L}(\mathbf{m})$ measuring the probability density of a model given data and a *posterior* pdf $\Sigma(\mathbf{m})$, which is given by

$$\Sigma(\mathbf{m}) = \kappa\rho(\mathbf{m})\mathcal{L}(\mathbf{m}), \tag{11}$$

where κ is a proportionality factor ensuring that the integral of $\Sigma(\mathbf{m})$ over the entire model space equals 1. Integrating $\Sigma(\mathbf{m})$ over a part of the model space corresponds to the probability that the true model $\mathbf{m}^*$ lies within that part, given data and prior information. Assuming

$$\mathcal{L}(\mathbf{m}) = \exp(-\phi_d(\mathbf{m})) \tag{12}$$

and

$$\rho(\mathbf{m}) = \exp(-\lambda\phi_m(\mathbf{m})), \tag{13}$$

a maximization of Σ becomes equivalent to a minimization of ϕ in the deterministic inversion.

4.2 Monte Carlo sampling

For a probabilistic inversion of the corrected C-responses, we use the Metropolis–Hastings algorithm (Metropolis *et al.* 1953; Hastings 1970), which was shown to be particularly efficient in sampling the posterior pdf. It can be described as follows (Mosegaard & Tarantola 1995):

Given a function $\mathcal{K}(\mathbf{m})$, which samples the prior pdf iteratively, and a uniformly distributed random number α drawn from the interval [0, 1], the model is updated as

$$\mathbf{m}_{k+1} = \begin{cases} \mathcal{K}(\mathbf{m}_k) & \text{if } \alpha \leq \min\left(1, \frac{\mathcal{L}(\mathcal{K}(\mathbf{m}_k))}{\mathcal{L}(\mathbf{m}_k)}\right), \\ \mathbf{m}_k & \text{else,} \end{cases} \tag{14}$$

with $\mathcal{L}(\mathbf{m})$ defined as in eq. (12). This algorithm generates successive samples of the posterior pdf without explicitly calculating $\Sigma(\mathbf{m})$. The sampling density is proportional to the probability density, that is, low-probability areas of the model space are sampled less excessively.

The critical aspect in the implementation of the Metropolis-Hastings algorithm is the function $\mathcal{K}(\mathbf{m})$, which is supposed to generate successive samples of the prior pdf. The constraints imposed upon the model in deterministic inversion (Section 3) are not easily applicable in Monte Carlo methods, and we do not formulate an explicit prior $\rho(\mathbf{m})$ as suggested by eq. (13). Based on laboratory measurements of anhydrous mantle mineral conductivities, Khan *et al.* (2011) assumed conductivity to be a non-decreasing function of depth. This strong constraint, however, yielded unrealistically small model uncertainties (not shown here for brevity). We therefore opted for the following constraints:

(i) Conductivity must not vary by more than one order of magnitude between adjacent layers,
(ii) Conductivity has to lie in the range $[10^{-5}\ \mathrm{S\,m^{-1}}; 10^{3}\ \mathrm{S\,m^{-1}}]$.

This yields upper and lower bounds for $m_j = \log_{10}(\sigma_j/\sigma_0)$, with $\sigma_0 = 1\ \mathrm{S\,m^{-1}}$. A random number generator was employed to pick a value between these bounds assuming a uniform distribution. The number of model parameters to be perturbed in an iteration according to the above constraints was adjusted to yield an overall acceptance rate of 40 per cent.

10^6 models were sampled in total. In Fig. 5, we present 400 near-independent samples of the posterior pdf, obtained by retaining only one sample every 1000 iterations. The collection of sampled models agrees well with the result of the deterministic inversion. The spread of the models is minimum at a depth of 1000 km and increases both at shallower and greater depths, in agreement with the uncertainty estimates of the deterministic inversion. The results of the Monte Carlo inversion, however, do not spread symmetrically around the result of the deterministic inversion. This is particularly the case in the top 800 km, where the Monte Carlo results tend to smaller conductivities.

5 DISCUSSION

Deterministic inversion is computationally cheap and therefore most often the preferred solution in large geophysical inverse problems. Comparison of our result to that of Kuvshinov & Olsen (2006) shows large differences in the top 800 km, where our model is significantly more resistive. The model of Kuvshinov & Olsen (2006) is generally smoother, which is most probably due to stronger regularization. The fact that the models partially differ by more than an order of magnitude is most likely due to data-related issues:

(i) The real part of our C-responses is larger at all periods, which is due to the fact that Kuvshinov & Olsen (2006) included a damping parameter when processing the raw data.

(ii) Kuvshinov & Olsen (2006) estimated *C*-responses at periods <1 day and therefore sampled shallower depths.

(iii) The effect of the correction for induction in the oceans is slightly more pronounced in our study (*cf.* Fig. 2).

In contrast to Kuvshinov & Olsen (2006), we provide model uncertainties, estimated from the inverse Hessian of the cost function. These uncertainties should rather be interpreted qualitatively than quantitatively, because their estimation is based on several approximations (*cf.* Section 3). Nevertheless, they provide good indications about the resolution and show that with current data in a period range from 1.5 to 150 d, sensitivity is maximum at depths between 800 and 1200 km. The most prominent feature of our results, the sharp edge at a depth of 900 km, lies in this well-resolved depth range and thus likely represents real structure.

Apart from the very apparent edge, the recovered model also shows a zone of elevated conductivity at a depth of approximately 900 km. This feature, however, is not very pronounced, and might actually be an artefact that arises from lack of information in the data. The estimated model uncertainties clearly allow for models without such a zone (Fig. 5) and hence confirm that this structure is not trustworthy.

Probabilistic approaches to inverse problems offer an alternative framework for analysing the reliability of a recovered model. The results of an independent Monte Carlo study, which relied on different prior information, agree well with those of the deterministic inversion. In particular, the sharp edge at a depth of 900 km is also visible in the results of the probabilistic inversion. The recovered models, however, tend to smaller conductivities in the upper mantle and show more structure in the lower mantle. This might indicate that the prior constraints used in the deterministic inversion are slightly stronger than those used in the probabilistic inversion. The Monte Carlo results also confirm the depth-dependency of the uncertainties obtained in the deterministic inversion. Only in the top 600 km, the upper bound of these uncertainties appears too large.

6 PRELIMINARY INTERPRETATION OF MANTLE CONDUCTIVITY STRUCTURE

To interpret the inverted conductivity profile (Fig. 5), we construct laboratory-based conductivity profiles as a function of mantle composition, temperature, pressure and water content. We combine laboratory measurements of mineral conductivity with a self-consistently computed mineralogical model of the Earth's mantle using Gibbs free-energy minimization following the approach outlined in Khan & Shankland (2012). For present purposes, we assume a chemically homogeneous and adiabatic mantle made of pyrolite. The bulk electrical conductivity profiles so computed are shown in Fig. 6 for different values of mantle water content (here restricted to be present in the minerals olivine (ol), orthopyroxene, wadsleyite (wads) and ringwoodite) and self-consistently computed mantle adiabats. Input temperature for the latter is defined as the temperature at the location where the mantle adiabat intersects the conductive geotherm at 150 km depth. For more details on constructing laboratory-based conductivity profiles, we refer the reader to Khan & Shankland (2012).

The discontinuities associated with mineral phase transformations at 410, 520 and 660 km depth are clearly present in the laboratory-based conductivity profiles, but absent in the field-derived profile. The inability of EM fields to sense discontinuities results directly from their diffusive nature. Conductivities found here in the upper mantle appear to be well-estimated by an upper mantle water content of 0.001 wt per cent and a mantle temperature of 1200 °C at 150 km depth in line with earlier observations (e.g. Karato 2011; Khan & Shankland 2012; Yoshino & Katsura 2013). In the absence of conductivity measurements of hydrous lower mantle minerals, the recovered edge of the conductivity profile at around 900 km depth either requires higher temperatures or the presence of material of higher conductivity such as that associated with ponding of melt in and below the transition zone.

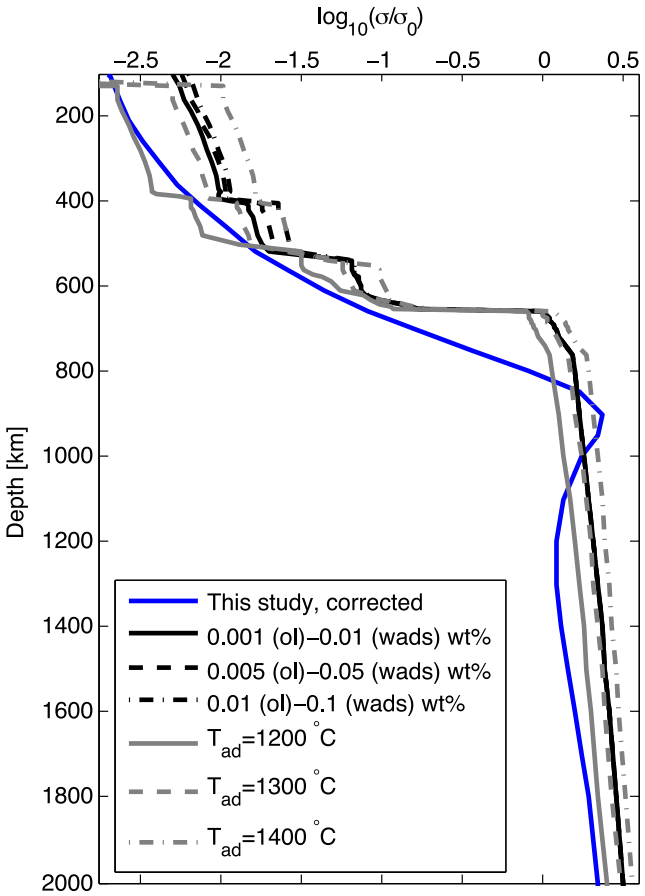

Figure 6. 1-D conductivity profiles estimated in this study (blue line) and computed using laboratory-based conductivity data for various mantle water contents and temperatures. Ol and wads refer to major upper mantle and transition-zone minerals olivine and wadsleyite, respectively. T_{ad} is the temperature at the location where the mantle adiabat intersects the conductive geotherm at 150 km depth. For the computations related to variations in water content (black lines), we assumed a mantle adiabat of 1300 °C with an intersection depth of 100 km, whereas for the mantle adiabats (grey lines) we fixed water content to 0.001 wt per cent (ol) and 0.01 wt per cent (wads). $\sigma_0 = 1$ S m^{-1}. See the main text for more details.

Recent geophysical studies suggest ponding of melt at the top of the lower mantle as a means of explaining some anomalous features. For example, in a regional 3-D EM study Koyama *et al.* (2014) found a strong conductivity anomaly underneath the south-eastern part of Australia at the bottom of the transition-zone that appears to require the presence of melt. Schmandt *et al.* (2014), using *P*-to-*S* conversions (receiver functions), likewise observed what appears to be evidence for melt below the transition-zone underneath the North American continent. Locally large conductivity anomalies in the topmost lower mantle might be related to carbonate melts, which have been observed experimentally to increase conductivity significantly beyond what is possible with hydrous olivine (e.g.

Gaillard *et al.* 2008; Yoshino *et al.* 2012). As discussed by, for example, Litasov (2011) melting in CO_2-containing systems can produce carbonate melts in these regions of the mantle. We leave it for future studies to consider this in more detail.

7 CONCLUSION AND OUTLOOK

Global *C*-responses were estimated from a vast amount of data that derive from satellites and geomagnetic observatories. We corrected the responses for 3-D effects due to induction in the oceans by an iterative approach.

The corrected *C*-responses were inverted for a 1-D electrical conductivity profile of Earth's mantle. The recovered model features a highly resistive upper mantle, increasing conductivity in and beneath the transition zone and high conductivities underneath. The results of a deterministic inversion were verified by a direct inversion of uncorrected responses in a 3-D environment and an independent probabilistic analysis. We showed that reasonable bounds for the recovered model can be obtained within the framework of a deterministic inversion by making use of the inverse Hessian of the cost function. The uncertainty estimates reveal that data are most sensitive to structures at depths between 800 and 1200 km, whereas conductivity at depths $<$400 km and $>$1600 km is poorly constrained.

An update of the conductivity model recovered in this study is planned once several years of data from the *Swarm* multisatellite geomagnetic mission will become available.

ACKNOWLEDGEMENTS

This work has been supported by the Swiss National Science Foundation under Grant No. 2000021-140711/1 and in part by the Russian Foundation for Basic Research under Grant No. 13-05-12111.

REFERENCES

Banks, R., 1969. Geomagnetic variations and the electrical conductivity of the upper mantle, *Geophys. J. R. astr. Soc.,* **17,** 457–487.

Chapman, S. & Price, A., 1930. The electric and magnetic state of the interior of the Earth as inferred from terrestrial magnetic variations, *Phil. Trans. R. Soc. Lond., A,* **229,** 427–460.

Civet, F. & Tarits, P., 2013. Analysis of magnetic satellite data to infer the mantle electrical conductivity of telluric planets in the solar system, *Planet. Space Sci.,* **84,** 102–111.

Civet, F., Thébault, E., Verhoeven, O., Langlais, B. & Saturnino, D., 2015. Electrical conductivity of the Earth's mantle from the first Swarm magnetic field measurements, *Geophys. Res. Lett.,* **42,** 3338–3346.

Constable, S. & Constable, C., 2004. Observing geomagnetic induction in magnetic satellite measurements and associated implications for mantle conductivity, *Geochem. Geophys. Geosyst.,* **5,** doi:10.1029/2003GC000634.

Didwall, E., 1984. The electrical conductivity of the upper mantle as estimated from satellite magnetic field data, *J. geophys. Res.,* **89,** 537–542.

Everett, M., Constable, S. & Constable, C., 2003. Effects of near-surface conductance on global satellite induction responses, *Geophys. J. Int.,* **153,** 277–286.

Friis-Christensen, E., Lühr, H. & Hulot, G., 2006. *Swarm*: A constellation to study the Earth's magnetic field, *Earth Planets Space,* **58,** 351–358.

Gaillard, F., Malki, M., Iacono-Marziano, G., Pichavant, M. & Scaillet, B., 2008. Carbonatite melts and electrical conductivity in the asthenosphere, *Science,* **322,** 1363–1365.

Hansen, P., 1992. Analysis of discrete ill-posed problems by means of the L-curve, *SIAM Rev.,* **34,** 561–580.

Hastings, W., 1970. Monte Carlo sampling methods using Markov chains and their applications, *Biometrika,* **57,** 97–109.

Karato, S., 2011. Water distribution across the mantle transition zone and its implications for global material circulation, *Earth planet. Sci. Lett.,* **301,** 413–423.

Khan, A. & Shankland, T., 2012. A geophysical perspective on mantle water content and melting: inverting electromagnetic sounding data using laboratory-based electrical conductivity profiles, *Earth planet. Sci. Lett.,* **317–318,** 27–34.

Khan, A., Kuvshinov, A. & Semenov, A., 2011. On the heterogeneous electrical conductivity structure of the Earth's mantle with implications for transition zone water content, *J. geophys. Res.,* **116,** doi:10.1029/2010JB007458.

Koyama, T., Khan, A. & Kuvshinov, A., 2014. Three-dimensional electrical conductivity structure beneath Australia from inversion of geomagnetic observatory data: evidence for lateral variations in transition-zone temperature, water content and melt, *Geophys. J. Int.,* **196,** 1330–1350.

Kuvshinov, A. & Olsen, N., 2005. Modelling the ocean effect of geomagnetic storms at ground and satellite altitude, in *Earth Observation with CHAMP. Results from Three Years in Orbit,* pp. 353–358, eds Reigber, C., Lühr, H., Schwintzer, P. & Wickert, J., Springer.

Kuvshinov, A. & Olsen, N., 2006. A global model of mantle conductivity derived from 5 years of CHAMP, Ørsted, and SAC-C magnetic data, *Geophys. Res. Lett.,* **33,** doi:10.1029/2006GL027083.

Kuvshinov, A. & Semenov, A., 2012. Global 3-D imaging of mantle electrical conductivity based on inversion of observatory *C*-responses—I. An approach and its verification, *Geophys. J. Int.,* **189,** 1335–1352.

Kuvshinov, A., Utada, H., Avdeev, D. & Koyama, T., 2005. 3-D modelling and analysis of *Dst C*-responses in the North Pacific Ocean region, revisited, *Geophys. J. Int.,* **160,** 505–526.

Lahiri, B. & Price, A., 1939. Electromagnetic induction in non-uniform conductors, and the determination of the conductivity of the Earth from terrestrial magnetic variations., *Phil. Trans. R. Soc. Lond., A,* **237,** 509–540.

Litasov, K., 2011. Physicochemical conditions for melting in the Earth's mantle containing a C-O-H fluid (from experimental data), *Geophys. Res. Lett.,* **52,** 475–492.

Metropolis, N., Rosenbluth, A., Rosenbluth, M., Teller, A. & Teller, E., 1953. Equation of state calculations by fast computing machines, *J. Chem. Phys.,* **21,** 1087–1092.

Mosegaard, K. & Tarantola, A., 1995. Monte Carlo sampling of solutions to inverse problems, *J. geophys. Res.,* **100,** 12 431–12 447.

Nocedal, J. & Wright, S., 2006. *Numerical Optimization,* Springer.

Olsen, N., 1998. The electrical conductivity of the mantle beneath Europe derived from *C*-responses from 3 to 720 hr, *Geophys. J. Int.,* **133,** 298–308.

Olsen, N., 1999. Induction studies with satellite data, *Surv. Geophys.,* **20,** 309–340.

Olsen, N., Lühr, H., Finlay, C., Sabaka, T., Michaelis, I., Rauberg, J. & Tøffner-Clausen, L., 2014. The CHAOS-4 geomagnetic field model, *Geophys. J. Int.,* **197,** 815–827.

Pankratov, O. & Kuvshinov, A., 2015. General formalism for the efficient calculation of the Hessian matrix of EM data misfit and Hessian-vector products based upon adjoint sources approach, *Geophys. J. Int.,* **200,** 1449–1465.

Pankratov, O., Avdeev, D. & Kuvshinov, A., 1995. Electromagnetic field scattering in a heterogeneous Earth: a solution to the forward problem, *Phys. Solid Earth,* **31,** 201–209.

Püthe, C. & Kuvshinov, A., 2013. Determination of the 1-D distribution of electrical conductivity in Earth's mantle from *Swarm* satellite data, *Earth Planets Space,* **65,** 1233–1237.

Püthe, C. & Kuvshinov, A., 2014. Mapping 3-D mantle electrical conductivity from space. A new 3-D inversion scheme based on analysis of matrix *Q*-responses, *Geophys. J. Int.,* **197,** 768–784.

Sabaka, T., Tøffner-Clausen, L. & Olsen, N., 2013. Use of the Comprehensive Inversion method for *Swarm* satellite data analysis, *Earth Planets Space,* **65,** 1201–1222.

Schmandt, B., Jacobsen, S., Becker, T., Liu, Z. & Dueker, K., 2014. Dehydration melting at the top of the lower mantle, *Science,* **344,** 1265–1268.

Schmucker, U., 1985a. Magnetic and electric fields due to electromagnetic induction by external sources, in *Landolt-Börnstein, New Series, 5/2b,* pp. 100–125, Springer.

Schmucker, U., 1985b. Sources of the geomagnetic field, in *Landolt-Börnstein, New Series, 5/2b,* pp. 31–73, Springer.

Schultz, A. & Larsen, J. C., 1987. On the electrical conductivity of the mid-mantle—I. Calculation of equivalent scalar magnetotelluric response functions, *Geophys. J. R. astr. Soc.,* **88,** 733–761.

Tarantola, A., 2005. *Inverse Problem Theory and Methods for Model Parameter Estimation,* SIAM.

Velímský, J., Martinec, Z. & Everett, M., 2006. Electrical conductivity in the Earth's mantle inferred from CHAMP satellite measurements—I. Data processing and 1-D inversion, *Geophys. J. Int.,* **166,** 529–542.

Weidelt, P., 1972. The inverse problem of geomagnetic induction, *Z. Geophys.,* **38,** 257–289.

Yoshino, T. & Katsura, T., 2013. Electrical conductivity of mantle minerals: role of water in conductivity anomalies, *Annu. Rev. Earth Planet. Sci.,* **41,** 605–628.

Yoshino, T., McIsaac, E., Laumonier, M. & Katsura, T., 2012. Electrical conductivity of partial molten carbonate peridotite, *Phys. Earth planet. Int.,* **194–195,** 1–9.

APPENDIX: ANALYTICAL COMPUTATION OF THE GRADIENT VECTOR AND THE HESSIAN MATRIX

Kuvshinov & Semenov (2012) discuss in the appendix of their paper the solution of Maxwell's equations in a spherical 1-D model consisting of N layers, in which conductivity σ varies with radius r as

$$\sigma(r) = \sigma_k \left(\frac{r_k}{r}\right)^2, \quad r_{k+1} < r < r_k, \tag{A1}$$

where $r_1 = a$, $r_{N+1} = 0$ and σ_k is an appropriate constant. Conductivity is thus a piecewise inverse quadratic function of depth. If the layers are thin, the variation of conductivity within a layer is small, thus $\sigma(r) \approx \sigma_k$ for $r_{k+1} < r < r_k$. Formulation (A1) however is mathematically easier to handle than a piecewise constant conductivity structure.

Kuvshinov & Semenov (2012) discuss the calculation of admittances $Y_k(\omega) = Y(\omega, r_k)$ in a spherical body with conductivity structure as given by eq. (A1). Admittances can be calculated analytically with a recurrence formula, that is, $Y_k = f(\sigma_k, Y_{k+1})$ and $Y_N = f(\sigma_N)$. Furthermore, the C-response is related to the admittance at Earth's surface as

$$C(\omega) = -\frac{1}{\mathrm{i}\omega\mu_0 Y_1(\omega)}, \tag{A2}$$

where μ_0 is the magnetic permeability of free space. The explicit recurrence formula, which is mathematically not complex, but cumbersome, is given in appendix E of Kuvshinov & Semenov (2012).

Descent methods used in deterministic inversions require the computation of the gradient and Hessian of the data misfit, which in our case is given by eq. (4). The gradient $\nabla\phi_d$ contains the derivatives of the misfit ϕ_d with respect to the model parameters m_k, which read

$$\frac{\partial\phi_d}{\partial m_k} = \frac{2}{N_\omega}\mathrm{Re}\sum_{\omega\in\Omega}\frac{(C^{\mathrm{mod}}(\omega) - C^{\mathrm{obs}}(\omega))^*}{\delta C^{\mathrm{obs}}(\omega)^2}\frac{\partial C^{\mathrm{mod}}(\omega)}{\partial m_k}, \tag{A3}$$

where superscript $*$ stands for complex conjugation. m_k is a function of the conductivities, which depends on the parametrization of the inversion domain. This function is usually simple — in our case, $m_k = \log_{10}(\sigma_k/\sigma_0)$, with $\sigma_0 = 1$ S m^{-1}. We concentrate on calculating the derivatives of $C^{\mathrm{mod}}(\omega)$ with respect to σ_k, the derivatives with respect to m_k follow with the chain rule. Taking in mind the recurrence formula, we obtain

$$\frac{\partial C}{\partial \sigma_k} = \frac{\partial C}{\partial Y_1}\prod_{i=1}^{k-1}\left(\frac{\partial Y_i}{\partial Y_{i+1}}\right)\frac{\partial Y_k}{\partial \sigma_k}, \tag{A4}$$

where, from eq. (A2),

$$\frac{\partial C}{\partial Y_1} = \frac{1}{\mathrm{i}\omega\mu_0 Y_1(\omega)^2}. \tag{A5}$$

The Hessian $\mathbf{H}(\phi_d)$ contains the second derivatives of the misfit ϕ_d with respect to the model parameters. Its components follow from eq. (A3),

$$\frac{\partial^2\phi_d}{\partial m_k \partial m_l} = \frac{2}{N_\omega}\mathrm{Re}\sum_{\omega\in\Omega}\left[\frac{(C^{\mathrm{mod}}(\omega) - C^{\mathrm{obs}}(\omega))^*}{\delta C^{\mathrm{obs}}(\omega)^2}\frac{\partial^2 C^{\mathrm{mod}}(\omega)}{\partial m_k \partial m_l} + \frac{1}{\delta C^{\mathrm{obs}}(\omega)^2}\left(\frac{\partial C^{\mathrm{mod}}(\omega)}{\partial m_k}\right)^*\frac{\partial C^{\mathrm{mod}}(\omega)}{\partial m_l}\right]. \tag{A6}$$

This equation contains the second derivative of the C-response with respect to the model parameters m_k and m_l. We again focus on the derivatives with respect to the conductivities. Taking the derivative of eq. (A4) with respect to σ_l, we obtain

$$\begin{aligned}\frac{\partial^2 C}{\partial\sigma_k\partial\sigma_l} = {} & \frac{\partial^2 C}{\partial Y_1^2}\prod_{i=1}^{l-1}\left(\frac{\partial Y_i}{\partial Y_{i+1}}\right)\frac{\partial Y_l}{\partial\sigma_l}\prod_{i=1}^{k-1}\left(\frac{\partial Y_i}{\partial Y_{i+1}}\right)\frac{\partial Y_k}{\partial\sigma_k} \\ & + \frac{\partial C}{\partial Y_1}\prod_{i=1}^{l-1}\left(\frac{\partial Y_i}{\partial Y_{i+1}}\right)\frac{\partial}{\partial\sigma_l}\left(\frac{\partial Y_l}{\partial Y_{l+1}}\right) \\ & \times\prod_{i=l+1}^{k-1}\left(\frac{\partial Y_i}{\partial Y_{i+1}}\right)\frac{\partial Y_k}{\partial\sigma_k} \\ & + \sum_{j=1}^{l-1}\left[\frac{\partial C}{\partial Y_1}\prod_{i=1}^{j-1}\left(\frac{\partial Y_i}{\partial Y_{i+1}}\right)\frac{\partial^2 Y_j}{\partial Y_{j+1}^2}\right. \\ & \left.\times\prod_{i=j+1}^{l-1}\left(\frac{\partial Y_i}{\partial Y_{i+1}}\right)\frac{\partial Y_l}{\partial\sigma_l}\prod_{i=j+1}^{k-1}\left(\frac{\partial Y_i}{\partial Y_{i+1}}\right)\frac{\partial Y_k}{\partial\sigma_k}\right]\end{aligned} \tag{A7}$$

for off-diagonal elements of $\mathbf{H}(\phi_d)$ (here assuming $l < k$, for $l > k$, indices must be switched). For diagonal elements, we obtain analogously

$$\begin{aligned}\frac{\partial^2 C}{\partial\sigma_k^2} = {} & \frac{\partial^2 C}{\partial Y_1^2}\left(\prod_{i=1}^{k-1}\left(\frac{\partial Y_i}{\partial Y_{i+1}}\right)\frac{\partial Y_k}{\partial\sigma_k}\right)^2 + \frac{\partial C}{\partial Y_1}\prod_{i=1}^{k-1}\left(\frac{\partial Y_i}{\partial Y_{i+1}}\right)\frac{\partial^2 Y_k}{\partial\sigma_k^2} \\ & + \sum_{j=1}^{k-1}\left[\frac{\partial C}{\partial Y_1}\prod_{i=1}^{j-1}\left(\frac{\partial Y_i}{\partial Y_{i+1}}\right)\frac{\partial^2 Y_j}{\partial Y_{j+1}^2}\right. \\ & \left.\times\left(\prod_{i=j+1}^{k-1}\left(\frac{\partial Y_i}{\partial Y_{i+1}}\right)\frac{\partial Y_k}{\partial\sigma_k}\right)^2\right].\end{aligned} \tag{A8}$$

From eq. (A2), we can again deduce that

$$\frac{\partial^2 C}{\partial Y_1^2} = -\frac{2}{\mathrm{i}\omega\mu_0 Y_1(\omega)^3}. \tag{A9}$$

The computation of all other derivatives appearing in eqs (A4), (A7) and (A8) requires the ingestion of the recurrence formula for Y_k (Kuvshinov & Semenov 2012) in the above equations.